

Generation of Nonspherical Liquid Metal Microparticles with Tunable Shapes Exhibiting an Electrostatic-Responsive Performance

Shiyu Wang,[†] Zhiqiang Zhu,[†] Canzhen Ma, Ran Qiao, Chaoyu Yang, Ronald X. Xu, and Ting Si*



Cite This: *ACS Appl. Mater. Interfaces* 2021, 13, 16677–16687



Read Online

ACCESS |

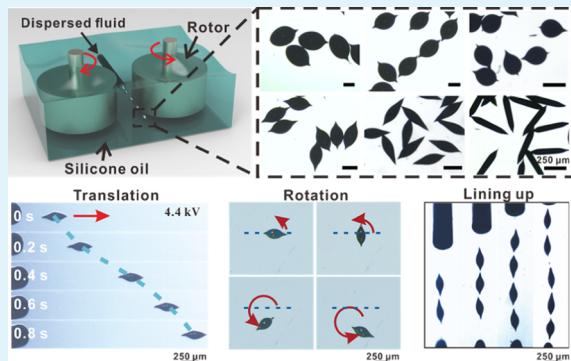
Metrics & More

Article Recommendations

Supporting Information

ABSTRACT: Nonspherical liquid metal microparticles (NLMs) show extraordinary potential in various applications due to their multifunctional and structural advantages. To one-step-produce shaped NLMs with high efficiency, high controllability, and free of template, a facile microfluidic strategy named rotary flow shearing (RFS) is reported. A high-speed viscous shearing flow is provided by two counter-rotating rotors in the carrier fluid, inducing continuous pinch-off of liquid metal flowing from a capillary tube positioned in face of the slit between two rotors. The real-time oxidation realizes the rapid solidification of the pinching neck and the liquid metal surface during the RFS process, resulting in massive NLMs. Different from other microfluidic methods, the RFS enables tunable shapes of NLMs, especially for working materials at high viscosities. The collected NLMs exhibit special electrostatic-responsive performances including translation, rotation, reciprocation, and lining up under the manipulation of an external electric field. Such NLMs can be promisingly used for the construction of novel micromotors and soft electronics.

KEYWORDS: liquid metal, nonspherical microparticles, electrostatic-responsive, micromotors, self-organized chains



1. INTRODUCTION

Room-temperature liquid metals (LMs) have received increasing attention in a variety of frontier engineering domains.^{1–4} In recent years, as nontoxic alternatives of mercury, gallium and gallium-based alloys including eutectic gallium–indium (EGaIn) and gallium–indium–tin (galinstan) possess excellent merits such as high thermal and electric conductivity, desirable biocompatibility, and photothermal effect.^{5,6} Therefore, Ga-based LMs have great potential in diverse areas, such as biomedicine, engineering materials, and energy.^{5,7–9} Especially fascinating are LM microparticles, which have served as outstanding platforms for constructing advanced functional materials and engineering devices.^{3,4,10,11}

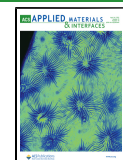
Previous studies have demonstrated that free-standing LM microparticles can be used as micromotors and soft electronics. Magnetic-responsive LM mobiles were fabricated by LM droplets encapsulating ferromagnetic particles.^{12,13} LM droplets placed on thin silver (Ag) films have been used as motors that could move along predefined paths at quite high velocities.¹⁴ Inspired by natural motile microorganisms, which meet their own survival needs through a variety of morphologies,¹⁵ functionalized LM motors with smart three-dimensional (3D) structures are facing a growing demand. Rodlike LM gallium nanomachines propelled by an ultrasound field have been fabricated, exhibiting the ability to actively seek and drill into the predefined HeLa cells.¹⁶ Dumbbell-like LM micromotors driven by elliptically polarized magnetic fields

have been fabricated, which display a novel motion mechanism with asymmetric wobbling.¹⁷ The electric actuation of LM droplets is typically conducted in an ionic electrolyte solution following the principle of electrochemistry.^{18–20} Besides, the electrostatic actuation of Hg microdroplets has been reported for the application of microswitches.^{21,22} Another important application of LM microparticles is the LM–elastomer composite, which is fabricated by mechanically mixing LMs with an elastomer.^{23–29} These LM microparticles embedded in a soft elastomer can deform along with the matrix and efficiently maintain their high electrical conductivity at high strains, which can be used as soft electronics and soft robots. Compared with conventional soft electronics, LM droplet-based composite electronics have displayed additional extraordinary properties such as self-healing and positive piezo-conductivity.^{23,24} The future development of LM-based elastomer composites with precise control of droplet size, shape, orientation, and arrangement may contribute to more capabilities.^{23,29}

Received: January 19, 2021

Accepted: March 26, 2021

Published: April 5, 2021



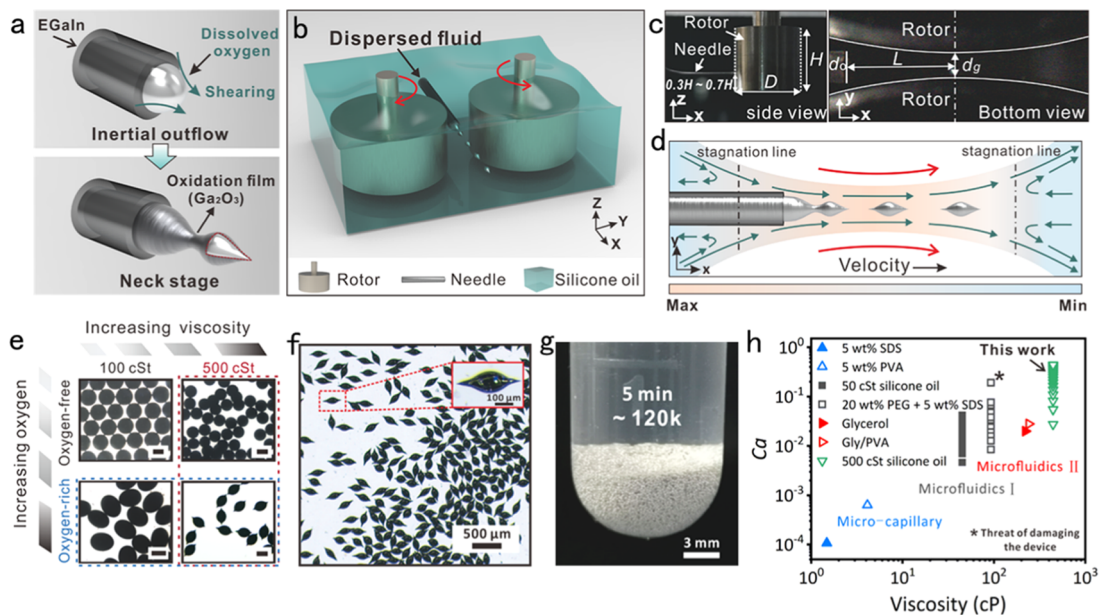


Figure 1. Generation of nonspherical LM microparticles (NLMs) by a simple but efficient rotary flow shearing (RFS) method. (a) The dynamic outflow shearing and the LM surface oxidation enable the formation of NLMs. (b) Schematic representation of the RFS process. (c) Side view (left) and bottom view (right) of an experimental RFS device with geometrical parameters: rotor diameter D , height H , outer needle diameter d_o , gap minimum width d_g , and distance L from the needle mouth to the gap with minimum width. (d) Schematic of streamlines within the slit, showing high velocities around the NLMs between two rotors. (e) Optical images of collected NLMs with varying silicone oil viscosities and oxygen solubilities. Scale bar: 500 μm . (f) Optical image of collected NLMs exhibiting sharp tails. (g) Massive NLMs collected within 5 min showing the production capacity of RFS. (h) Parametric map showing the comparison between this work and previous methods in the LM droplet generation.

Room-temperature LMs usually have the tendency to retain their spherical shape to minimize the surface free energy due to the high surface tension. However, it is particularly important to maintain the LM droplets in nonequilibrium shapes, according to the passivating oxide film rapidly formed on the LM surface in contact with oxygen.^{30,31} The self-limited LM oxide film (commonly several nm) hardly changes the rheological properties of LM and it is able to mechanically maintain the nonspherical shape of NLMs.^{10,32} Particular shapes often give extra functionality to NLM. For instance, different from LM nanospheres, LM nanorods with asymmetrical ends can swim in a rotational style in water by acoustic energy, which make them capable of drilling into the cell.¹⁶ NLMs exhibit fantastic performances in specific applications. In the field of biomedicine, some NLMs have shown capacities of killing cancer cells and pathogens.^{7,16}

Prefabricated templates or microfluidic channels are usually used to mold LMs into specific shapes.^{16,17,33,34} In the case of metal part casting, crimson molten metal is poured into a mold of particular shapes and left to cool for solidification. In previous studies, the formation of shaped NLMs usually follows a similar strategy, trying to split bulk LMs into microparticles, shape them by external geometrical constraints, and stabilize morphologies by the formed oxide layer. Such approaches relying on external geometric restriction to form shaped NLMs have the limitations of low efficiency, low throughput, and low morphology optionality.^{34,35} There are still many challenges in the preparation of shaped NLMs, which also limit their practical applications.

In this work, we report a simple yet efficient microfluidic approach named rotary flow shearing (RFS) to one-step-generate shaped NLMs. The special morphology of NLMs originates from the typical capillary pinch-off with a thinning

“neck” connecting two neighboring droplets during droplet generation in Polydimethylsiloxane (PDMS) microchannels and glass microcapillaries. However, the RFS method enables tunable shapes and precise size of NLMs, especially for working fluids at high viscosities and high velocities, far different from these traditional microfluidic ones. Besides, due to the unique self-shaping fabrication strategy without additional molds or constraint channels, the RFS device can be easily scaled up for massive production of NLMs. More interestingly, NLMs exhibit unique individual and group movement behaviors under an external electric field, contributing to the control of position and arrangement of LM particles. Such NLMs with uniform sizes can be used as excellent units to construct periodic structures, which have enormous potential for developing complex functional composite materials with unique optical, electrical, or mechanical properties.^{23,36,37}

2. RESULTS AND DISCUSSION

2.1. Generation of NLMs in Carried Fluid with High Viscosity.

In a typical microchannel flow process, the droplet formation arises from the shrinking (thinning and elongation) of the neck connecting the main drop with the remaining fluid at the exit, which is often governed by the Rayleigh–Plateau instability.³⁸ Before the singularity fracture, the neck region retains the form of a double cone, endowing newly formed droplets with an instantaneous nonspherical feature of remarkable conelike tails.^{39,40} Without shaping droplets through external geometrical restrictions, a novel way to form shaped NLMs is to utilize the self-deformation behavior of LM in the capillary pinch-off stage existing in microfluidic technologies. However, due to the interfacial tension of fluids and the relatively low velocity of capillary flows in these

microfluidic devices, the newly formed droplets will quickly gain a spherical shape. Although the tail rapidly retracts and is short-lived, it is technically feasible to “capture” this finite-time pinching-derived morphology of LMs by utilizing the mechanical stability of the LM oxide skin (Figure 1a). The present study aims to find an efficient way to produce NLMs with different length–diameter ratios by matching the oxide film formation time and the pinch-off time, ensuring the solidification of the droplets during the pinch-off process.

Capillary flows are capable of steadily and smoothly stretching fluid interfaces down to the micrometric dimension and below.⁴¹ The fluid dynamic force fields usually include pressure, inertia, and viscosity. In this work, we propose the rotary flow shearing (RFS) method to fabricate LM (EGaIn) microparticles, utilizing the shearing flow of the continuous phase induced by the rotation of a set of counter-rotating rotors to break the EGaIn supplied through a capillary tube, as shown in Figure 1a–d. This RFS strategy is particularly advantageous for employing working materials at high velocity and high viscosity (i.e., with high inertia force and viscous force), and the commonly used silicone oil can serve as an ideal carrier fluid to realize the coupling of pinching and oxidation processes in LM microparticle formation for two crucial properties: high oxygen solubility and high viscosity. It has been reported that the oxygen solubility (25 °C) in silicone oil is about 60 times higher than that in water,⁴² which can cause the rapid formation of the oxide skin on the surface of LM.³⁵ In addition to oxide film generation, another key factor of shape formation is the pinch-off time, namely, the time taken for the droplet to separate from the nozzle. In this stage, the neck region, which connects the main droplet to the residue, gradually thins by the fluid flowing upward and downward out of the neck due to increasing curvature-induced pressure.⁴³ Therefore, the necking process was governed by the capillary and viscous forces, in which the capillary forces facilitate the thinning of the neck, while the viscous resistance tends to resist thinning and contraction of the pinching neck.⁴⁴ Owing to the extremely high surface tension (~7.7 times higher than water), the pinch-off time of LM is commonly too short to match the formation of the oxide layer. Hence, it is necessary to delay the necking time by increasing the viscosity of the external continuous flow, which is of great significance for the retention of the cone after the pinching neck fracture (Figure S2, Supporting Information).

In an RFS device, the counter-rotating cylindrical rotors and the needle (or capillary tube) are all submerged in a wide-open container filled with silicone oil (Figure 1b). An electro-mechanical system (the details of the structure are shown in Figure S1, Supporting Information) is constructed to ensure that two rotors rotate at the same velocity in opposite directions. The slit between two rotors has a dumbbell-like configuration along the cross section ($x-y$ plane) perpendicular to the rotor axis. A blunt needle is stuck into the flow inlet of the slit and placed along the central axis (Figure 1c). By rotating the rotors at a constant rotational speed ω (rpm), the slit between two rotors works as an open self-driving microchannel inducing the high-speed flow of the continuous phase because of its viscosity (Figure 1d). The flow field of the continuous phase around the rotors can be directly obtained according to a numerical simulation (Figure S1, Supporting Information), which indicates that in addition to the unidirectional shearing flow in the middle part of the gap region, there are backflows near the areas a little far away from

the narrowest gap, as demarcated by the area between two stagnation lines in Figure 1d. Therefore, it is necessary to place the tip of the needle close to the rotors’ slit to realize the “flow focusing”-like droplet generation.^{45–47} In our experiment, we adopt the 34 G stainless-steel needle (outer diameter $d_o = 320 \mu\text{m}$, inner diameter $d_i = 171 \mu\text{m}$) and two tungsten–steel cylinder rotors ($D = 12.84 \text{ mm}$), and select $L = 1.17 \text{ mm}$ and $d_g = 260 \mu\text{m}$ to realize the experimental prototype (Figure 1c).

The effects of oxygen and viscosity synergy of carrier fluid on the RFS process for the formation of LM microparticles are first verified at a relatively low rotational speed of 350 rpm and an LM flow rate of $50 \mu\text{L min}^{-1}$. For deoxygenated silicone oil, the formed LM microparticles have a spherical shape even when the viscosity of oil increases from 100 to 500 cSt. For oxygen-rich oil with low viscosity (100 cSt), the formed LM microparticles exhibit nonspherical shapes (ellipsoidal) with no tails retained, and for oxygen-rich oil with high viscosity (500 cSt), NLMs with tapering tails can be fabricated. The microscopic images of the collected LM microparticles are given in Figure 1e. As the rotational speed increases up to 500 rpm, NLMs with two conelike tapered sharp tails can be obtained in 500 cSt silicone oil (Figure 1f). We further demonstrate that the NLMs can always remain stable in the oil. A long-term test has been performed and there is no obvious change in the NLM morphology even after storing for 30 days (Figure S3, Supporting Information). Owing to the robustness of the RFS process, it is easy to realize the massive production (~24 000 per min in a single-needle device) of tailed NLMs (Figure 1g), and the throughput can be improved dramatically by the scale-up of the system. It should be mentioned that high-viscosity fluids are generally avoided in conventional microfluidic methods, as the high pressure induced within the microchannel would potentially damage the devices.^{48,49} However, the RFS process can adopt the carrier fluid with extremely high viscosity (e.g., 500 cSt silicone oil), and the flow field in the vicinity of rotors’ slit is locally concentrated, independent of the device walls, providing a strong shearing force one to two orders of magnitude higher than the conventional microfluidic methods. In comparison with previous methods of producing LM droplets,^{33,35,50} this is the first time that such a carrier fluid with extremely high viscosity (e.g., 500 cSt) has been reported in microfluidic flows (Figure 1h).

2.2. RFS Process Control for NLM Formation. In the RFS process for producing LM microparticles, the controllable parameters mainly include the rotational speed of rotors ω , the LM flow rate Q , and the viscosity of silicone oil μ when the geometric parameters are kept constant. The profile of a pinching neck involves a balance between capillary, viscous, and inertia forces in the two fluids,⁵¹ as characterized by the nondimensional parameters, i.e., the capillary number $Ca = \frac{\pi \mu \omega D}{\sigma}$, which is the ratio between viscous force and capillary force, and the Weber number $We = \frac{4\rho Q^2 d_o}{\pi^2 d_i^4}$ for the ratio between inertia force and capillary force, where the interfacial tension between oil and EGaIn $\sigma = 542.146 \text{ mN m}^{-1}$, the density of EGaIn $\rho = 6.28 \text{ g cm}^{-3}$, $d_o = 320 \mu\text{m}$, $d_i = 171 \mu\text{m}$, and $D = 12.84 \text{ mm}$. To ensure LM surface oxidation, the carrier fluid silicone oil is filled with oxygen to saturation for several minutes before each experimental run.

In experiments, we have captured the formation of LM microparticles in the RFS process using a high-speed video

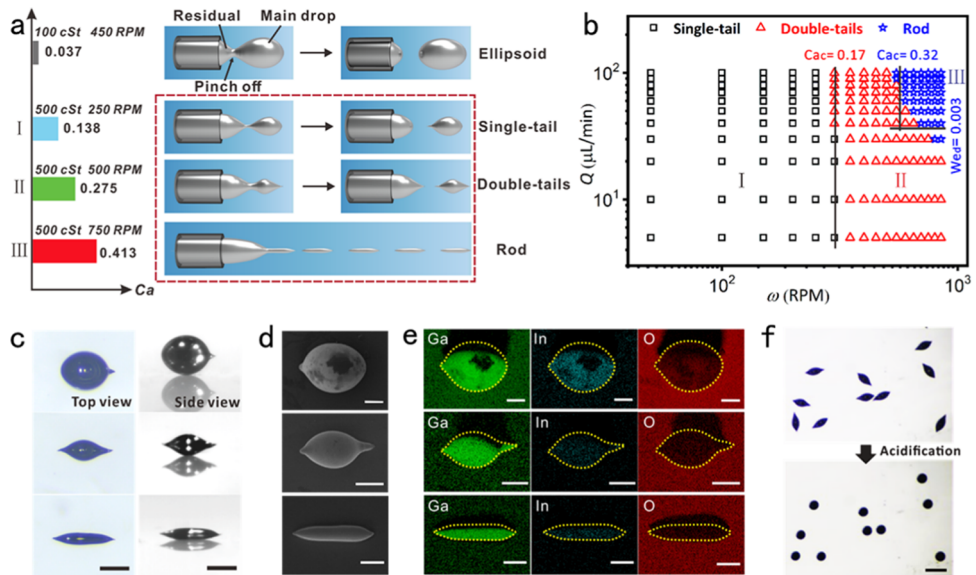


Figure 2. Morphologies and shape design of NLMs in the RFS process. (a) Effects of silicone oil viscosities and rotor rotating rates on the RFS process to form NLMs with shapes of the ellipsoid, single tail, double tail, and rod. (b) Experimental ω - Q phase diagram showing the transitions among different modes. (c) Optical images of the top view (left) and side view (right), (d) scanning electron microscopy (SEM) images, and (e) EDS mapping images showing the presence of gallium, indium, and oxygen for three types of NLMs. (f) Optical images showing the release of double-tail NLMs to a spherical shape because of acidification. Scale bar: (c) 200 μm , (d–e) 100 μm , and (f) 500 μm .

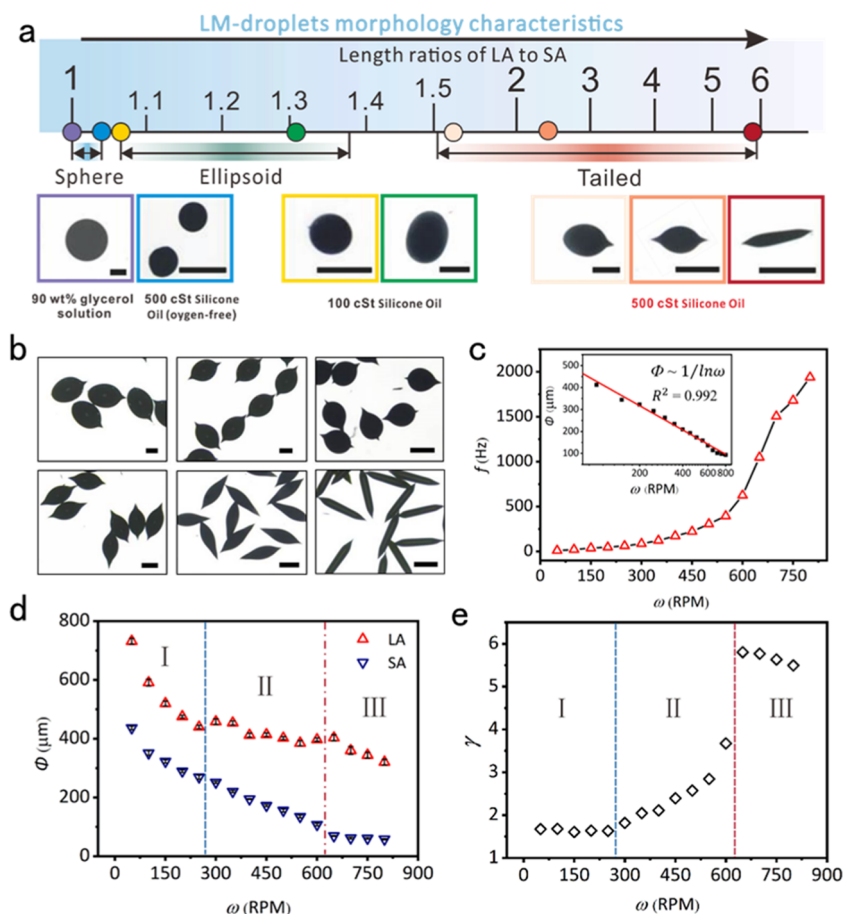


Figure 3. Parametric effects on the shapes of NLMs. (a) Schematic of the NLM morphology with different length ratios γ of the long axis (LA) to the short axis (SA). (b) Micrographs of various NLMs as the value of γ increases. (c) Formation frequency of NLMs as a function of rotating rate ω . Inset image: NLM sizes calculated from spherical droplets after acidification. (d) Lengths of LA and SA, and (e) the length ratio γ versus the rotating rate ω . Scale bar: (a) 300 μm and (b) 250 μm .

camera and identified different flow stages and their regimes under various parameters (Video S1, Supporting Information). For the low-viscosity carrier fluid (e.g., 100 cSt silicone oil), the LM pinch-off results in the main drop, and the residual LM has a slight retraction at the needle mouth in each period. The main drop turns into an ellipsoid without tails even when the value of ω is relatively high (e.g., 450 rpm). For the high-viscosity carrier fluid (e.g., 500 cSt silicone oil), the formation of NLMs mainly involves three different stages (labeled stage I, stage II, stage III) as the value of ω increases, resulting in diverse features of products with single-tail, double-tail, and rod shapes, and the conelike tails are very sharp (see Figure 2a–d). These unprecedented shapes of NLMs are derived from the LM pinch-off in the shear flow, associated with a tug-of-war behavior between two cones in the vicinity of the narrowest point whose position is pulled to the winner's side.⁵² The experimental phase diagram is shown in Figure 2b. It can be seen that the single-tail NLMs are generated in the case of low rotational speed ω (stage I, $Ca < 0.17$). On further increasing ω , the formed NLMs switch from a single tail to a double tail after a transition point of about $Ca = 0.17$ (stage II). Impressively, as the values of Ca and We increase (stage III, $Ca > 0.32$ and $We > 0.003$), the shape of generated NLMs changes significantly, exhibiting a rodlike structure. The increase of Ca (improving ω) indicates the increase of the viscous shearing effect to overcome the inhibition of droplet deformation caused by the interfacial tension.^{33,49,53}

The morphologies of NLMs are further characterized. Microscopic images show that the shape of NLMs is nearly axisymmetric with respect to their long axis due to the axisymmetric capillary pinch-off process (Figure 2c). Scanning electron microscopy (SEM) images in Figure 2d demonstrate the solidification of NLMs with three typical shapes in the air. Note that the conelike ends of NLMs became blunt after they were extracted into the air, probably because of the organic solvent volatilization during the extraction process. Energy-dispersive X-ray spectroscopy (EDS) is further conducted to confirm the composition of NLMs. The corresponding EDS mapping images illustrate the presence of oxygen in the NLMs (Figure 2e, where the area outside the yellow outline in the right column shows a greater oxygen distribution than that on the droplet surface, derived from silica glass as the substrate), confirming the formation of gallium oxide (Ga_2O_3). Gallium is oxidized more easily than indium within EGaIn for the larger decrease of Gibbs free energy.⁵⁴ The EDS scanning area (green area) cannot cover the entire surface of the droplet because of the limited field of view, and there is a dark area behind the droplet without scanning in the mapping diagram (Figure S4, Supporting Information).

To further demonstrate the shape stabilization of NLMs protected by the outer oxide film, double-tail NLMs are transferred from the oil phase to the water phase at pH = 7 with the original morphology remaining (see the upper part of Figure 2f). By adding hydrochloric acid to the water until pH = 5, the double-tail NLMs are completely transformed into a spherical shape after 3 min at 25 °C, as the outer Ga_2O_3 can be decomposed in an acidic condition (see the lower part of Figure 2f). This shape transformation, once the oxide layers are removed, results from the presence of the high surface tension of inner EGaIn cores.¹⁶ These results imply that the produced NLMs exhibit good adaptability in various pH-neutral conditions (oil, water, and air) and pH-responsive deformability.

2.3. Effect of Parameters on NLM Morphology. To highlight the significant morphology characteristics of NLMs, we have measured the length–diameter aspect ratio (γ) of the long axis (LA) to the short axis (SA) of diverse LM microparticles composed of the sphere, ellipsoid, and three typical NLMs (single tail, double tail, and rod), as shown in Figure 3a. The LM spheres are fabricated in oxygen-free silicone oil with an aspect ratio $\gamma = 1$. Ellipsoid LM microparticles are produced in oxygen-rich silicone oil with low viscosity (100 cSt), with an aspect ratio γ of between 1.06 and 1.37. In this case, as the value of ω increases, the aspect ratio γ decreases until the shape of LM microparticles becomes nearly spherical (Figure S5, Supporting Information). For oxygen-rich silicone oil with high viscosity (500 cSt), NLMs with the presence of a tail greatly enlarge the aspect ratio, ranging from 1.6 to 5.8 and even higher.

The shapes of NLMs can be modified regularly by tuning the values of ω and Q continuously. For the EGaIn/silicone oil (500 cSt) fluid system, uniform NLMs can be generated steadily in a range of control parameters for $Q = 10\text{--}100 \mu\text{L min}^{-1}$ and $\omega = 50\text{--}800 \text{ rpm}$, respectively. Generally, the size of NLMs increases with the increase of Q and the decrease of ω . As the value of ω increases for fixed Q , microscopic images of formed NLMs are as shown in Figure 3b. It can be seen that the morphologies of NLMs change in sequence from the single tail, double tail to rod shapes. For simplification, we have transformed NLMs into LM spheres via acidification (Figure 2f) and measured the diameters of the samples normalized in shape. By plotting and fitting the experimental data, the relationship between the droplet size (Φ) and the rotational speed (ω) can be written as

$$\Phi \sim \left(\frac{Q}{f} \right)^{-1/3} \sim \frac{1}{\ln \omega} \quad (1)$$

which implies that the droplet size will decrease as the rotational speed increases by keeping the flow rate constant. Therefore, the corresponding frequency f of droplet formation will increase dramatically, as shown in Figure 3c. Compared with most previous work, the RFS method significantly improves the production efficiency of LM microdroplets with particular shapes.^{53,55,56}

The influences of ω on the lengths of LA and SA and the aspect ratio (γ) of NLMs are determined, as shown in Figure 3d–e. By keeping the flow rate Q at a constant value of $50 \mu\text{L min}^{-1}$, we gradually increase the rotational speed ω from 50 to 800 rpm. The changes of LA and SA for NLMs in different formation stages follow different laws. With the increase of ω , both LA and SA decrease in the beginning (stage I), LA hardly changes, and SA continues to decrease in the intermediate ω range (stage II), and LA decreases while SA remains nearly constant beyond a threshold rotational speed (stage III). This demonstrates three different regimes of the droplet generation process.

The influence of Q on NLM morphology is a little different. The microscopic images of formed NLMs at different flow rates are shown in Figure S6, Supporting Information. In stage I, the increase of Q will increase both the lengths of LA and SA. For example, keeping $\omega = 250 \text{ rpm}$, with increasing Q from 50 to $100 \mu\text{L min}^{-1}$, the length of LA and SA increases by $55 \mu\text{m}$. As the flow rate reaches its maximum, the largest droplet can be formed in stage I. When $Q = 100 \mu\text{L min}^{-1}$ and $\omega = 50 \text{ rpm}$, the maximum size of droplets (single tail) can be $\sim 750 \mu\text{m}$ for

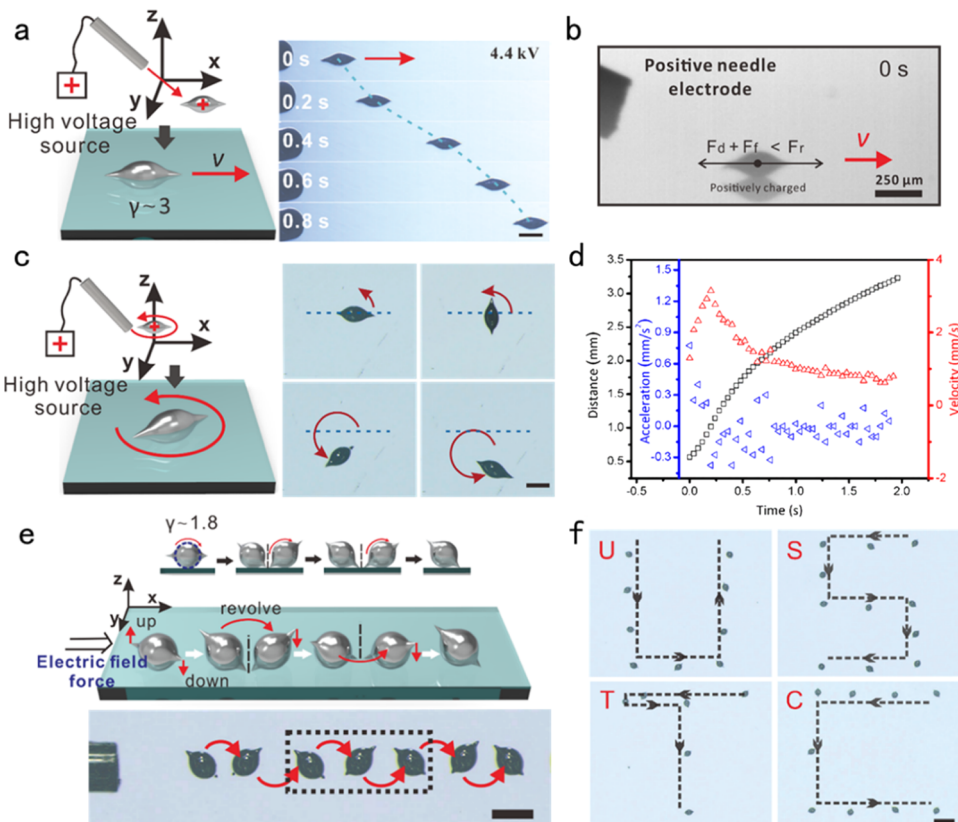


Figure 4. Motion of individual NLM triggered by electrostatic repulsion. (a) Directional motion and (b) locomotion mechanism of a double-tail NLM with $\gamma \sim 3$. (c) Rotation of a double-tail NLM with $\gamma \sim 3$. (d) The moving distance of NLM with $\gamma \approx 3$ continues to increase with time, while the velocity of the droplet initially increases, then decreases, and tends to become stable. The blue triangle dots represent the acceleration of NLM during the movement. (e) Special swinging rolling motion of a double-tail NLM with $\gamma \sim 1.8$. (f) Track of a double-tail NLM with $\gamma \sim 1.8$, forming a “USTC” pattern. Scale bar: (a, c, e) 250 μm and (f) 1 mm.

the long axis (LA) and 440 μm for the short axis (SA). In stage II, with the increase of Q , only the length of LA increases. In stage III, it is interesting to note that the change of Q has no significant influence on the size and morphology of the rod NLMs, which implies that in stage III, the yield of NLMs can be greatly improved by increasing the flow rate Q . The reason may lie in the fact that the shearing force mainly dominates the LM pinch-off process, which exhibits “jetting” behavior for a relatively high rotational speed ω of counter-rotating rotors, leading to different values of the minimum sizes of LA and SA under different conditions. When $Q = 10 \mu\text{L min}^{-1}$ and $\omega = 800$ rpm, NLM (double tails in stage II) exhibits a minimum LA of $\sim 260 \mu\text{m}$ and SA of $\sim 150 \mu\text{m}$. When $Q = 40 \mu\text{L min}^{-1}$ and $\omega = 800$ rpm, NLM (rod in stage III) exhibits a minimum LA of $\sim 310 \mu\text{m}$ and SA of $\sim 60 \mu\text{m}$.

2.4. Electrostatic-Responsive Performance of NLMs. Due to the high conductivity and the anisotropic structure of NLMs, it is feasible to employ NLMs as potential micromotors that can be manipulated using electrostatic fields. Compared with single-tail and rod NLMs, double-tail NLMs possess a relatively symmetrical structure and a spherelike bottom surface, resulting in higher balance and lower sliding friction in motion. The efficient propulsion of a single NLM ($\gamma \approx 3$) in 20 cSt silicone oil is realized by a needle-electrode-driving procedure, as shown in Figure 4a. A high-voltage needle electrode (a flat-end needle connected to a high-voltage power supply) is positioned above the substrate and approaches the NLM, which is quickly charged by the contact with the

electrode. The motion of the NLM is triggered by the electrostatic repulsion on a slippery quartz surface. Some other insulating liquids can also serve as ambient liquids. Under the electrostatic field from the needle electrode, double-tail NLMs with different morphologies can exhibit different behavioral characteristics. This large aspect ratio micromotor (long NLMs) displays a straight translational sliding movement, with the direction of tip alignment becoming almost the same as the propulsion direction (see Figure 4a). Besides, due to the electric directivity, the micromotor can rotate by changing the electric field direction (see Figure 4c). It is also observed that the rod NLMs exhibit similar motion characteristics to those of large aspect ratio ones.

The electrostatic force increases as the distance between the electrode and the particle decreases. To promote the motion of a single NLM on the substrate, the needle electrode gradually approaches the NLM, reaching a certain distance, for enough electrostatic repulsion F_r to overcome the static friction force F_f and the medium viscous resistance F_d (see Figure 4b). To understand the motion characteristics of the particle under this mechanism, we have analyzed the motion of the particle propelled by electrostatic repulsion with 4.4 kV direct-current voltage (see Figure 4d), whose motion can be divided into two stages. In the initial stage, the electrostatic propulsion force is larger than the total resistance, and a jump of velocity is obtained soon after the micromotor moves, with the highest velocity of $\sim 3.3 \text{ mm s}^{-1}$. As the LM micromotor gradually moves away from the electrode at a short distance, the

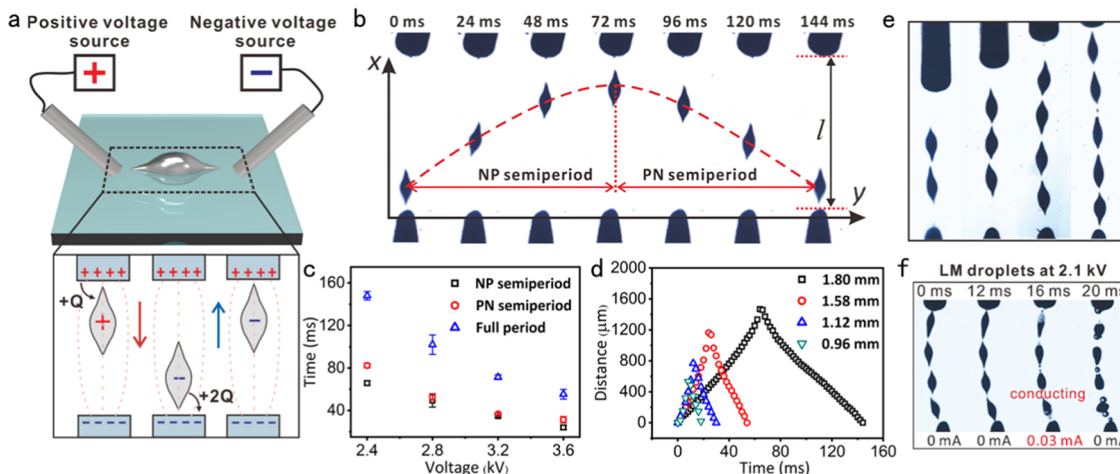


Figure 5. Reciprocation and self-arrangement of NLMs under an electrostatic field. (a) Schematic of repetitive charging/discharging for a double-tail NLM and (b) sequential experimental photographs of a reciprocating period between positive and negative electrodes. (c) Durations of PN and NP semiperiods and a total period as a function of the applied voltage. (d) Plots of NLM moving distance as a function of time during a period with changing distances between electrodes (0.96, 1.12, 1.58, 1.80 mm). (e) Experimental images of multiple NLM chains without contact. (f) Sequential photographs of the NLM chain self-regulation process including break-over and electrolysis at an applied voltage of 2.1 kV after contact.

electrostatic repulsion force reduces to a value less than the resistance force, resulting in a decreasing speed of the droplet in the second stage, maintaining a basically steady speed of $\sim 1 \text{ mm s}^{-1}$ for a period of 1–2 s. The particle velocity can be adjusted by changing the applied electric voltage. The tail on one side of the droplet always tends to point in the direction of the electric field during movement, which is related to the uneven charge distribution inside the NLM. The higher surface charge density on the region near the cone tip enhances the local electric field, making the long axis of the motor continuously follow the electric field to keep the force balance.

Differing from the motion characteristics of NLMs with large aspect ratios, NLMs with relatively small aspect ratios (short NLMs) cannot maintain the directional sliding motion when a single needle electrode approaches the NLM from one side. We choose a roller-shaped NLM ($\gamma \approx 1.8$) as an experimental object, which exhibits a crawl-like motion. A superimposed snapshot of the moving process within a certain period is shown in Figure 4e. Because the main body of the short NLM is approximately spherical, the NLM tends to roll away instead of sliding under the effect of electrical repulsion force. While the NLM is rolling, the two tails, by turns, rub against the substrate at an angle, making the micromotor “crawl” along the electric field direction. By controlling the path of the needle electrode, we can control the single NLM to move in a predefined trajectory (Figure 4f). Compared with the sliding mechanism, this peculiar rolling mechanism causes most of the surface of the droplet to periodically come into contact with the substrate, which can be applied in some future microrobots relying on surface sensors to perform detection tasks.

To achieve accurate manipulation of the micromotor between two fixed positions, we add a grounded needle electrode to the previous single-electrode controlling system, as shown in Figure 5a. Two needle electrodes, one connected to the positive high voltage supply and the other to the ground, are immersed in silicone oil at an oblique angle, respectively, with their tips touching the bottom surface of the quartz container. It can be found that the double-tail NLM maintains reciprocating motion between two electrodes, with a long axis

almost keeping parallel to the electric field (Figure 5b and Video S2, Supporting Information). The continuously reciprocating movement comes from the repetitive charging/discharging processes between the NLM and electrodes.⁵⁷ The positive electrode endows NLM with positive charges at the start, resulting in the translational movement from the positive electrode to the grounded electrode. Once the NLM touches the negatively charged ground electrode, the charge on the droplet becomes negative, making the droplet come back to the positive electrode and then recharge again. This charging/discharging process is repeated until the applied voltage becomes zero. Figure 5b shows sequential photographs (24 ms per frame) of a reciprocating period of a tailed NLM, where the process of the particle motion from the negative electrode to the positive electrode is called the NP semiperiod and the converse process is called the PN semiperiod. Figure 5c shows the relationship between the motion time of the micromotor and the applied voltages. On increasing the applied voltage from 2.4 to 3.6 kV, both PN and NP semiperiods decrease, resulting in a significant drop of the total duration from 148 to 55 ms, which illustrates the rapid increase of the travel velocity in a higher-strength electrostatic field. It should be mentioned that there is a small time difference between PN and NP semiperiods at a low voltage of 2.4 kV, which may be caused by the slightly asymmetric shape of the micromotor. As the applied voltage increases, the effect of small shape asymmetry on the NLM movement becomes negligible. The motion trajectory of NLM during a period is plotted in Figure 5d by changing the distance between two electrodes ($l = 0.96, 1.12, 1.58, 1.80 \text{ mm}$). It can be seen that the period of the NLM movement decreases as the value of l decreases, and the NLM movement follows similar rules.

The well-organized swarm motion mode of tiny motors is vital to building a smart robot system for performing specific tasks.^{58,59} In this work, the movement behaviors of a group of NLMs under an electrostatic field are also investigated. It is interesting that the NLMs initially placed between two electrodes in random positions quickly arrange in a tip-to-tip line. This phenomenon is caused by the nonuniform electric field between electrodes, where the particles get polarized and

experience the dielectrophoresis (DEP) action.⁶⁰ The DEP force is determined by the polarizability of particles, which makes the particles align into a line.⁶¹ However, this procedure cannot be performed in noninsulating liquid because of the risk of charge leakage and short circuit. The length of the chains can be easily increased by introducing increasingly more NLMs by further increasing the distance between two needle electrodes, as shown in Figure 5e. The NLM chain consists of multiple NLMs trapped by the electrical field, and each of them maintains a dynamic process of oscillation, alternately colliding with the adjacent one (see Video S3, Supporting Information). As long as the distance between two electrodes is much larger than the total length of multiple NLMs in the tip-to-tip line, the well-organized swarm motion mode can be maintained for a long time because the current path cannot be formed. Inserting a positive needle electrode into a container where NLMs abound, there are arranged NLM chains between the needle electrode and the surrounding wall. This phenomenon is derived from the container wall acting as a negative electrode. Besides, because the current path cannot be formed, the arranged droplets can maintain their morphologies for a long time (Figure S7, Supporting Information). A similar procedure can also be performed in materials with higher viscosities (e.g., diluted PDMS, 10³ cSt) (Figure S8, Supporting Information). The formed NLMs can be diluted and evenly dispersed in PDMS, with well-maintained morphologies (Figure S9, Supporting Information).

Once all NLMs of the chain touch end to end and are in contact with the positive and negative electrodes, a connecting circuit is created, resulting in the electrolysis of the oxide film on the surface of the NLMs. A dramatic transient electrifying phenomenon of the NLM dynamic chain is presented in Figure 5f, accompanied by the NLM shape transformation and oxygen release in the energization stage. The electrolysis process begins at the contact points of the particles, probably due to the large resistance at the tips of the tails. In the dynamic self-regulation process of the NLM chain, oxygen is released through oxidation film electrolysis, and the morphology of NLMs can no longer be maintained. The NLM chain can serve as an electrical circuit due to its self-organized arrangement in a line, and then quickly disconnect owing to the contraction of the NLMs. This electrolysis phenomenon of NLMs due to their connection under an electrostatic field would be useful for soft electronics applications.

3. CONCLUSIONS

A facile and compatible microfluidic droplet generation strategy, named rotary flow shearing (RFS), is developed to rapidly produce shaped nonspherical LM microparticles (NLMs) with typical conelike tails. The shape and size of NLMs can be controlled by altering the rotational speed ω of rotors and the flow rate Q of EGaIn. The NLMs possess unique electrostatic-responsive characteristics. Triggered by electrostatic repulsion, the NLMs with large and small aspect ratios exhibit different motion behaviors, respectively. By applying a unidirectional electric field, double-tail NLMs can serve as simple electrostatic micromotors in reciprocating tip-to-tip dynamic motion between positive and negative electrodes. Given the special shapes and electrostatic-responsive arrangement characteristics of NLMs, the construction of novel micromotors and soft electronics may benefit from NLMs with controllable size and arrangement.

4. EXPERIMENTAL SECTION

4.1. Materials. EGaIn (75% Ga, 25% In) was purchased from Santech Materials Co., Ltd. (Changsha, China). Petroleum ether, ethanol, and glycerol were purchased from Sinopharm Chemical Reagent Co., Ltd. (Shanghai, China). Poly(vinyl alcohol) (PVA) and silicone oils were supplied by Sigma-Aldrich (St. Louis, MO). 184 Silicone Elastomer Curing Agent and SYLGARD® 184 Silicone Elastomer Base were purchased from Dow Corning (American). Deionized water was produced by the Millipore Direct-Q system.

4.2. Fabrication of the LM Droplet Generator. The droplet generation part was fabricated by aligning a 34 G stainless-steel blunt needle (inner and outer diameters of 171 and 320 μm , respectively; length of 37 mm) fixed on the resin needle holder (fabricated by 3D printing) to the gap between two symmetric tungsten–steel cylinders (diameter and length of 12.84 and 12 mm, respectively). We use a 3D guide rail attached to the needle holder to adjust the distance (maintained at 1.3 mm) between the 34 G needle and the axis of the symmetric cylinders. The tungsten–steel rotors (rotor R1 and rotor R2) consisted of a cylinder and shaft (diameter and length of 5 and 70 mm, respectively) that were formed integrally, and the cylinder was fixed at the end of the shaft. The shaft of the rotor R1 was driven by a direct-current (DC) motor. A pair of transmission gears (1:1) were fixed on the shafts of the rotor R1 and rotor R2, respectively, which were properly jointed to keep the R1 and R2 rotating at the same rotational speed in opposite directions. The speed of the motors ω was controlled using a pulse-width-modulation (PWM) motor controller. The motor and rotors were assembled on an aluminum U support frame, in which the assembly holes were all inserted with ball bearings to reduce friction and maintain the rotation perpendicular to the shaft axis. The supporting structure was assembled from four stainless-steel support pins, an optical flat (30 cm \times 30 cm), and a PMMA frame produced using a laser cutter.

4.3. Preparation of the Oxygen-Free Silicone Oil. Silicone oil with viscosities of 100 and 500 cSt were used. Oxygen-free silicone oil was obtained by bubbling nitrogen through the oil for 3 h to wipe off the dissolved oxygen.

4.4. Preparation of the Aqueous Glycerol Solution. An aqueous solution of 90 wt % glycerol in deionized water was prepared by mixing and shaking and left overnight to dissolve completely.

4.5. Extraction of NLMs. The NLMs in the silicone oil can be transferred into water or air. After removing the supernatant oil, the collected NLMs were washed four times with petroleum ether, followed by four washes in ethanol and rinsing in deionized water. Parts of cleaned NLMs were left to dry; others were immediately preserved in a 2 wt % PVA aqueous solution to prevent sample fusion.

4.6. Construction of the Electrostatic Control System. The electrical field was generated by charged 34 G needle electrodes. The DC voltages were all provided by a high DC power supply (ES30P-SW, γ). The NLM formation processes were monitored by a charge-coupled device (CCD, DFK 23G274, Imaginsource) camera and captured by a high-speed camera (V2512, Phantom) with the help of a microscopic lens. To characterize the morphologies and element contents of the as-prepared samples, scanning electron microscopy (SEM) and energy-dispersive X-ray (EDS) element mapping were performed by field emission scanning electron microscopy (Genimi SEM 500, ZEISS). Optical microscopic images and videos were taken by an inverted microscope (Eclipse Ts2, Nikon) and a stereomicroscope (SZX7, Olympus) equipped with a CCD camera (MSX2-H, Mshot). Viscosity measurements were performed at 25 °C using a viscometer (LVDV-1T, Shanghai Performance Tai Electronic Technology Co., Ltd., China). Interfacial tension measurements of EGaIn in silicone oil (oxygen-rich and oxygen-free) were performed at 25 °C using a contact angle meter (XG-CAM, Shanghai Xuanyichuangxi Industrial Equipment Co., Ltd., China). Size statistics of formed LM droplets were performed by software ImageJ.

ASSOCIATED CONTENT

SI Supporting Information

The Supporting Information is available free of charge at <https://pubs.acs.org/doi/10.1021/acsami.1c01026>.

Formation process of rod NLMs by RFS (Video S1) ([MP4](#))

Reciprocating motion of isolated NLMs between positive and negative electrodes (Video S2) ([MP4](#))

Dynamic NLM chains between positive and negative electrodes (Video S3) ([MP4](#))

Detailed design of the platform and associated numerical simulation; high-viscosity silicone oil helps to preserve the tail of LM droplets; microscopic images showing long-term stability of the EGaIn sample in oil, EDS layered images; production of axiolitic LM micro-droplets; controlling the size of the formed NLMs by varying flow speed Q ; translational motion of double-tail NLMs with larger aspect ratios; and self-assembly of double-tail NLMs ([PDF](#))

AUTHOR INFORMATION

Corresponding Author

Ting Si – Department of Modern Mechanics, University of Science and Technology of China, Hefei, Anhui 230026, China;  orcid.org/0000-0001-9071-8646; Email: tsi@ustc.edu.cn

Authors

Shiyu Wang – Department of Precision Machinery and Precision Instrumentation and Key Laboratory of Precision Scientific Instrumentation of Anhui Higher Education Institutes, University of Science and Technology of China, Hefei, Anhui 230026, China

Zhiqiang Zhu – Department of Precision Machinery and Precision Instrumentation and Key Laboratory of Precision Scientific Instrumentation of Anhui Higher Education Institutes, University of Science and Technology of China, Hefei, Anhui 230026, China;  orcid.org/0000-0002-1277-5917

Canzhen Ma – Department of Precision Machinery and Precision Instrumentation and Key Laboratory of Precision Scientific Instrumentation of Anhui Higher Education Institutes, University of Science and Technology of China, Hefei, Anhui 230026, China

Ran Qiao – Department of Modern Mechanics, University of Science and Technology of China, Hefei, Anhui 230026, China

Chaoyu Yang – Department of Precision Machinery and Precision Instrumentation and Key Laboratory of Precision Scientific Instrumentation of Anhui Higher Education Institutes, University of Science and Technology of China, Hefei, Anhui 230026, China

Ronald X. Xu – Department of Biomedical Engineering, The Ohio State University, Columbus, Ohio 43210, United States;  orcid.org/0000-0003-2486-5677

Complete contact information is available at: <https://pubs.acs.org/doi/10.1021/acsami.1c01026>

Author Contributions

¹S.W. and Z.Z. contributed equally to this work.

Notes

The authors declare no competing financial interest.

ACKNOWLEDGMENTS

This work was supported by the National Natural Science Foundation of China (Nos. 12027801, 11621202, and 52003263), the Youth Innovation Promotion Association CAS (No. 2018491), the Anhui Provincial Natural Science Foundation (1908085QE200), the Strategic Priority Research Program of the Chinese Academy of Sciences (XDB22040103), the Science and Technology Program of Shenzhen (JSGG20180504165551779), and the Fundamental Research Funds for the Central Universities.

REFERENCES

- (1) Dickey, M. D. Emerging applications of liquid metals featuring surface oxides. *ACS Appl. Mater. Interfaces* **2014**, *6*, 18369–18379.
- (2) Cheng, S.; Wu, Z. Microfluidic electronics. *Lab Chip* **2012**, *12*, 2782–2791.
- (3) Khoshmanesh, K.; Tang, S. Y.; Zhu, J. Y.; Schaefer, S.; Mitchell, A.; Kalantar-Zadeh, K.; Dickey, M. D. Liquid metal enabled microfluidics. *Lab Chip* **2017**, *17*, 974–993.
- (4) Zhu, L.; Wang, B.; Handschuh-Wang, S.; Zhou, X. Liquid Metal-Based Soft Microfluidics. *Small* **2020**, *16*, No. 1903841.
- (5) Yan, J.; Lu, Y.; Chen, G.; Yang, M.; Gu, Z. Advances in liquid metals for biomedical applications. *Chem. Soc. Rev.* **2018**, *47*, 2518–2533.
- (6) Li, X.; Li, M.; Zong, L.; Wu, X.; You, J.; Du, P.; Li, C. Liquid Metal Droplets Wrapped with Polysaccharide Microgel as Biocompatible Aqueous Ink for Flexible Conductive Devices. *Adv. Funct. Mater.* **2018**, *28*, No. 1804197.
- (7) Elbourne, A.; Cheeseman, S.; Atkin, P.; Truong, N. P.; Syed, N.; Zavabeti, A.; Mohiuddin, M.; Esrafilzadeh, D.; Cozzolino, D.; McConvile, C. F.; Dickey, M. D.; Crawford, R. J.; Kalantar-Zadeh, K.; Chapman, J.; Daeneke, T.; Truong, V. K. Antibacterial Liquid Metals: Biofilm Treatment via Magnetic Activation. *ACS Nano* **2020**, *14*, 802–817.
- (8) Teng, L.; Ye, S.; Handschuh-Wang, S.; Zhou, X.; Gan, T.; Zhou, X. Liquid Metal-Based Transient Circuits for Flexible and Recyclable Electronics. *Adv. Funct. Mater.* **2019**, *29*, No. 1808739.
- (9) Tang, W.; Jiang, T.; Fan, F. R.; Yu, A. F.; Zhang, C.; Cao, X.; Wang, Z. L. Liquid-Metal Electrode for High-Performance Triboelectric Nanogenerator at an Instantaneous Energy Conversion Efficiency of 70.6%. *Adv. Funct. Mater.* **2015**, *25*, 3718–3725.
- (10) Daeneke, T.; Khoshmanesh, K.; Mahmood, N.; de Castro, I. A.; Esrafilzadeh, D.; Barrow, S. J.; Dickey, M. D.; Kalantar-Zadeh, K. Liquid metals: fundamentals and applications in chemistry. *Chem. Soc. Rev.* **2018**, *47*, 4073–4111.
- (11) Dickey, M. D. Stretchable and Soft Electronics using Liquid Metals. *Adv. Mater.* **2017**, *29*, No. 1606425.
- (12) Liu, H.; Li, M.; Li, Y.; Yang, H.; Li, A.; Lu, T. J.; Li, F.; Xu, F. Magnetic steering of liquid metal mobiles. *Soft Matter* **2018**, *14*, 3236–3245.
- (13) Jeon, J.; Lee, J. B.; Chung, S. K.; Kim, D. On-demand magnetic manipulation of liquid metal in microfluidic channels for electrical switching applications. *Lab Chip* **2017**, *17*, 128–133.
- (14) Mohammed, M.; Sundaresan, R.; Dickey, M. D. Self-Running Liquid Metal Drops that Delaminate Metal Films at Record Velocities. *ACS Appl. Mater. Interfaces* **2015**, *7*, 23163–71.
- (15) Walker, D.; Kasdorf, B. T.; Jeong, H. H.; Lieleg, O.; Fischer, P. Enzymatically active biomimetic micropropellers for the penetration of mucin gels. *Sci. Adv.* **2015**, *1*, No. e1500501.
- (16) Wang, D.; Gao, C.; Wang, W.; Sun, M.; Guo, B.; Xie, H.; He, Q. Shape-Transformable, Fusible Rodlike Swimming Liquid Metal Nanomachine. *ACS Nano* **2018**, *12*, 10212–10220.
- (17) Liu, M.; Wang, Y.; Kuai, Y.; Cong, J.; Xu, Y.; Piao, H. G.; Pan, L.; Liu, Y. Magnetically Powered Shape-Transformable Liquid Metal Micromotors. *Small* **2019**, *15*, No. 1905446.
- (18) Tang, S. Y.; Sivan, V.; Khoshmanesh, K.; O'Mullane, A. P.; Tang, X.; Gol, B.; Eshtiaghi, N.; Lieder, F.; Petersen, P.; Mitchell, A.;

- Kalantar-zadeh, K. Electrochemically induced actuation of liquid metal marbles. *Nanoscale* **2013**, *5*, 5949–5957.
- (19) Handschuh-Wang, S.; Chen, Y.; Zhu, L.; Gan, T.; Zhou, X. Electric Actuation of Liquid Metal Droplets in Acidified Aqueous Electrolyte. *Langmuir* **2019**, *35*, 372–381.
- (20) Hu, L.; Wang, L.; Ding, Y.; Zhan, S.; Liu, J. Manipulation of Liquid Metals on a Graphite Surface. *Adv. Mater.* **2016**, *28*, 9210–9217.
- (21) Kim, J.; Shen, W. J.; Latorre, L.; Kim, C. J. A micromechanical switch with electrostatically driven liquid-metal droplet. *Sens. Actuators, A* **2002**, *97*–*98*, 672–679.
- (22) Latorre, L.; Kim, J.; Lee, J.; de Guzman, P. P.; Lee, H. J.; Nouet, P.; Kim, C. J. Electrostatic actuation of microscale liquid-metal droplets. *J. Microelectromech. Syst.* **2002**, *11*, 302–308.
- (23) Markvicka, E. J.; Bartlett, M. D.; Huang, X.; Majidi, C. An autonomously electrically self-healing liquid metal-elastomer composite for robust soft-matter robotics and electronics. *Nat. Mater.* **2018**, *17*, 618–624.
- (24) Yun, G.; Tang, S. Y.; Sun, S.; Yuan, D.; Zhao, Q.; Deng, L.; Yan, S.; Du, H.; Dickey, M. D.; Li, W. Liquid metal-filled magneto-rheological elastomer with positive piezoconductivity. *Nat. Commun.* **2019**, *10*, No. 1300.
- (25) Feng, P.; Ji, H.; Zhang, L.; Luo, X.; Leng, X.; He, P.; Feng, H.; Zhang, J.; Ma, X.; Zhao, W. Highly stretchable patternable conductive circuits and wearable strain sensors based on polydimethylsiloxane and silver nanoparticles. *Nanotechnology* **2019**, *30*, No. 185501.
- (26) Nesaei, S.; Cavanagh, D. J.; Gozen, A. Rheology of liquid metal particle-based polymer composites: A comparative study. *J. Rheol.* **2019**, *63*, 559–568.
- (27) Park, S.; Thangavel, G.; Parida, K.; Li, S.; Lee, P. S. A Stretchable and Self-Healing Energy Storage Device Based on Mechanically and Electrically Restorative Liquid-Metal Particles and Carboxylated Polyurethane Composites. *Adv. Mater.* **2019**, *31*, No. 1805536.
- (28) Tutika, R.; Kmiec, S.; Haque, A.; Martin, S. W.; Bartlett, M. D. Liquid Metal-Elastomer Soft Composites with Independently Controllable and Highly Tunable Droplet Size and Volume Loading. *ACS Appl. Mater. Interfaces* **2019**, *11*, 17873–17883.
- (29) Haque, A. B. M. T.; Tutika, R.; Byrum, R. L.; Bartlett, M. D. Programmable Liquid Metal Microstructures for Multifunctional Soft Thermal Composites. *Adv. Funct. Mater.* **2020**, *30*, No. 2000832.
- (30) Dickey, M. D.; Chiechi, R. C.; Larsen, R. J.; Weiss, E. A.; Weitz, D. A.; Whitesides, G. M. Eutectic Gallium-Indium (EGaIn): A Liquid Metal Alloy for the Formation of Stable Structures in Microchannels at Room Temperature. *Adv. Funct. Mater.* **2008**, *18*, 1097–1104.
- (31) Chiechi, R. C.; Weiss, E. A.; Dickey, M. D.; Whitesides, G. M. Eutectic gallium-indium (EGaIn): a moldable liquid metal for electrical characterization of self-assembled monolayers. *Angew. Chem. Int. Ed.* **2008**, *47*, 142–4.
- (32) Regan, M. J.; Tostmann, H.; Pershan, P. S.; Magnussen, O. M.; DiMasi, E.; Ocko, B. M.; Deutsch, M. X-ray study of the oxidation of liquid-gallium surfaces. *Phys. Rev. B* **1997**, *55*, 10786–10790.
- (33) Lin, P.; Wei, Z.; Yan, Q.; Xie, J.; Fan, Y.; Wu, M.; Chen, Y.; Cheng, Z. Capillary-Based Microfluidic Fabrication of Liquid Metal Microspheres toward Functional Microelectrodes and Photothermal Medium. *ACS Appl. Mater. Interfaces* **2019**, *11*, 25295–25305.
- (34) Jin, T.; Hadji, E. M.; Zhao, N.; Duan, Z.; Wang, J. Generation and Analysis of Axiolitic Liquid-Metal Droplets in a T-Junction Microfluidic Device. *ChemistrySelect* **2019**, *4*, 3926–3935.
- (35) Hutter, T.; Bauer, W.-A. C.; Elliott, S. R.; Huck, W. T. S. Formation of Spherical and Non-Spherical Eutectic Gallium-Indium Liquid-Metal Microdroplets in Microfluidic Channels at Room Temperature. *Adv. Funct. Mater.* **2012**, *22*, 2624–2631.
- (36) Hashimoto, M.; Mayers, B.; Garstecki, P.; Whitesides, G. M. Flowing lattices of bubbles as tunable, self-assembled diffraction gratings. *Small* **2006**, *2*, 1292–8.
- (37) Yu, J. Q.; Yang, Y.; Liu, A. Q.; Chin, L. K.; Zhang, X. M. Microfluidic droplet grating for reconfigurable optical diffraction. *Opt. Lett.* **2010**, *35*, 1890–2.
- (38) Utada, A. S.; Fernandez-Nieves, A.; Gordillo, J. M.; Weitz, D. A. Absolute instability of a liquid jet in a coflowing stream. *Phys. Rev. Lett.* **2008**, *100*, No. 014502.
- (39) Li, H.; Mei, S.; Wang, L.; Gao, Y.; Liu, J. Splashing phenomena of room temperature liquid metal droplet striking on the pool of the same liquid under ambient air environment. *Int. J. Heat Fluid Flow* **2014**, *47*, 1–8.
- (40) Yu, Y.; Wang, Q.; Yi, L. T.; Liu, J. Channelless Fabrication for Large-Scale Preparation of Room Temperature Liquid Metal Droplets. *Adv. Eng. Mater.* **2014**, *16*, 255–262.
- (41) Barrero, A.; Loscertales, I. G. Micro- and Nanoparticles via Capillary Flows. *Annu. Rev. Fluid Mech.* **2007**, *39*, 89–106.
- (42) Xu, A.; He, B.; Yu, H.; Han, W.; Li, J.; Shen, J.; Sun, X.; Wang, L. A facile solution to mature cathode modified by hydrophobic dimethyl silicon oil (DMS) layer for electro-Fenton processes: Water proof and enhanced oxygen transport. *Electrochim. Acta* **2019**, *308*, 158–166.
- (43) Davidson, M. R.; Cooper-White, J. J. Pendant drop formation of shear-thinning and yield stress fluids. *Appl. Math. Modell.* **2006**, *30*, 1392–1405.
- (44) Kim, E.; Baek, J. Numerical study on the effects of non-dimensional parameters on drop-on-demand droplet formation dynamics and printability range in the up-scaled model. *Phys. Fluids* **2012**, *24*, No. 082103.
- (45) Mu, K.; Si, T.; Ding, H. Nonlinear dynamics and manipulation of dripping in capillary flow focusing. *Sci. China-Phys. Mech. Astron.* **2019**, *62*, No. 124713.
- (46) Mu, K.; Si, T.; Li, E.; Xu, R. X.; Ding, H. Numerical study on droplet generation in axisymmetric flow focusing upon actuation. *Phys. Fluids* **2018**, *30*, No. 012111.
- (47) Mu, K.; Qiao, R.; Guo, J.; Yang, C.; Wu, Y.; Si, T. Parametric study on stability and morphology of liquid cone in flow focusing. *Int. J. Multiphase Flow* **2020**, *135*, No. 103507.
- (48) Zhang, Y.; Tang, S.-Y.; Zhao, Q.; Yun, G.; Yuan, D.; Li, W. High-throughput production of uniformly sized liquid metal micro-droplets using submerged electrodispersion. *Appl. Phys. Lett.* **2019**, *114*, No. 154101.
- (49) Tang, S.-Y.; Wang, K.; Fan, K.; Feng, Z.; Zhang, Y.; Zhao, Q.; Yun, G.; Yuan, D.; Jiang, L.; Li, M.; Li, W. High-Throughput, Off-Chip Microdroplet Generator Enabled by a Spinning Conical Frustum. *Anal. Chem.* **2019**, *91*, 3725–3732.
- (50) Thelen, J.; Dickey, M. D.; Ward, T. A study of the production and reversible stability of EGaIn liquid metal microspheres using flow focusing. *Lab Chip* **2012**, *12*, 3961–3967.
- (51) Lister, J. R.; Stone, H. A. Capillary breakup of a viscous thread surrounded by another viscous fluid. *Phys. Fluids* **1998**, *10*, 2758–2764.
- (52) Zhang, W. W.; Lister, J. R. Similarity solutions for capillary pinch-off in fluids of differing viscosity. *Phys. Rev. Lett.* **1999**, *83*, 1151–1154.
- (53) Tang, S. Y.; Joshipura, I. D.; Lin, Y.; Kalantar-Zadeh, K.; Mitchell, A.; Khoshmanesh, K.; Dickey, M. D. Liquid-Metal Microdroplets Formed Dynamically with Electrical Control of Size and Rate. *Adv. Mater.* **2016**, *28*, 604–9.
- (54) Li, Z.; Zhang, H.; Wang, D.; Gao, C.; Sun, M.; Wu, Z.; He, Q. Reconfigurable Assembly of Active Liquid Metal Colloidal Cluster. *Angew. Chem., Int. Ed.* **2020**, *59*, 19884–19888.
- (55) Fang, W.-Q.; He, Z.-Z.; Liu, J. Electro-hydrodynamic shooting phenomenon of liquid metal stream. *Appl. Phys. Lett.* **2014**, *105*, No. 134104.
- (56) Tian, L.; Gao, M.; Gui, L. A Microfluidic Chip for Liquid Metal Droplet Generation and Sorting. *Micromachines* **2017**, *8*, No. 39.
- (57) Lee, S.; Lee, S.; Hwang, H.; Hong, J.; Lee, S.; Lee, J.; Chae, Y.; Lee, T. Ultrafast single-droplet bouncing actuator with electrostatic force on superhydrophobic electrodes. *RSC Adv.* **2016**, *6*, 66729–66737.
- (58) Chen, S.; Ding, Y.; Zhang, Q.; Wang, L.; Liu, J. Controllable dispersion and reunion of liquid metal droplets. *Sci. China Mater.* **2019**, *62*, 407–415.

- (59) Sheng, L.; He, Z.; Yao, Y.; Liu, J. Transient State Machine Enabled from the Colliding and Coalescence of a Swarm of Autonomously Running Liquid Metal Motors. *Small* **2015**, *11*, 5253–5261.
- (60) Hermanson, K. D.; Lumsdon, S. O.; Williams, J. P.; Kaler, E. W.; Velev, O. D. Dielectrophoretic assembly of electrically functional microwires from nanoparticle suspensions. *Science* **2001**, *294*, 1082–1086.
- (61) Krisnadi, F.; Nguyen, L. L.; Ankit; Ma, J.; Kulkarni, R.; Mathews, N.; Dickey, M. D. Directed Assembly of Liquid Metal-Elastomer Conductors for Stretchable and Self-Healing Electronics. *Adv. Mater.* **2020**, *32*, No. 2001642.